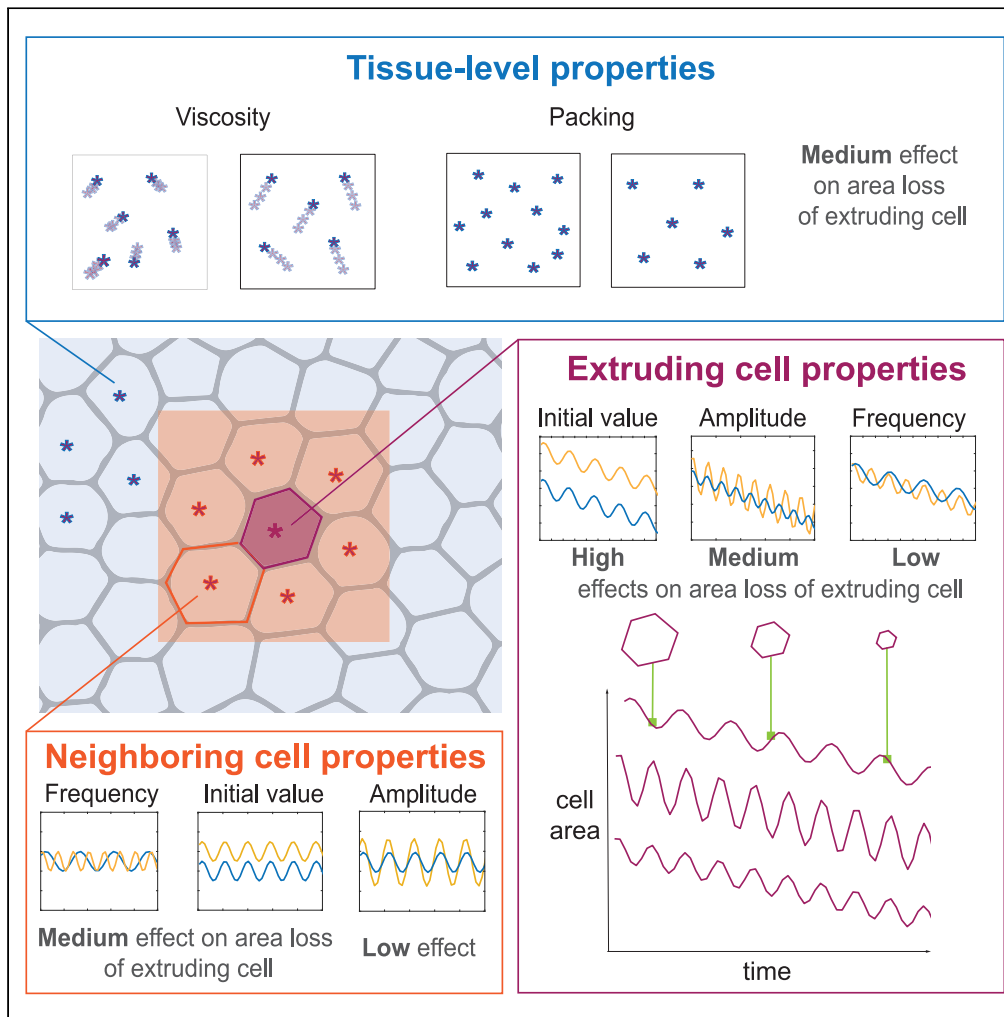## Article

Assessing mechanical agency during apical apoptotic cell extrusion

Sommer Anjum, Llaran Turner, Youmna Atieh, George T. Eisenhoffer, Lance A. Davidson

gteisenhoffer@mdanderson. org (G.T.E.)
lad43@pitt.edu (L.A.D.)

Highlights
An active particle model recapitulates oscillatory apoptotic cell extrusion

Assessment of biophysical properties of extruding cells, neighbors, and tissue

Identification of phase of extrusion marked by mechanical resistance to neighbors

Cell autonomous mechanics is the major contributor to extrusion dynamics

Article

Assessing mechanical agency during apical apoptotic cell extrusion

Sommer Anjum,[1,2] Llaran Turner,[3,4] Youmna Atieh,[3] George T. Eisenhoffer,[3,4,*] and Lance A. Davidson[1,5,6,7,*]

SUMMARY

Homeostasis is necessary for epithelia to maintain barrier function and prevent the accumulation of defective cells. Unfit, excess, and dying cells in the larval zebrafish tail fin epidermis are removed via controlled cell death and extrusion. Extrusion coincides with oscillations of cell area, both in the extruding cell and its neighbors. Here, we develop a biophysical model of this process to explore the role of autonomous and non-autonomous mechanics. We vary biophysical properties and oscillatory behaviors of extruding cells and their neighbors along with tissue-wide cell density and viscosity. We find that cell autonomous processes are major contributors to the dynamics of extrusion, with the mechanical microenvironment providing a less pronounced contribution. We also find that some cells initially resist extrusion, influencing the duration of the expulsion process. Our model provides insights into the cellular dynamics and mechanics that promote elimination of unwanted cells from epithelia during homeostatic tissue maintenance.

INTRODUCTION

Cell extrusion is critical for the maintenance of epithelial tissues,[1] as dysregulation of cell extrusion can disrupt epithelial barrier function and drive formation of adenocarcinomas.[2] Key modes of homeostatic cell extrusion include apoptotic cell extrusion, extrusion of transformed cells, and extrusion of live cells after overcrowding.[3–5] An inducible *in vivo* experimental system for apoptotic cell extrusion was recently developed in the epithelium of the larval zebrafish tail fin.[6] This epidermis is best classified as a squamous-type epithelium. Transgenic fish express the genetically encoded enzyme nitroreductase (NTR) in a subset of cells of the larval epidermis, and addition of the prodrug metronidazole (MTZ) creates a cytotoxic byproduct that promotes cells to be extruded. We collected high resolution time-lapse sequences of extruding epidermal cells and quantified geometric parameters of both extruding cells and their neighbors before, during, and after extrusion. Cells in NTR/MTZ-activated epithelia undergo a series of actomyosin-driven pulsatile contractions that result in oscillations of cell area that can be characterized by amplitude and duration. Area oscillations in extruding cells are additionally regulated by sphingosine-1-phosphate (S1P) and activation of a caspase cascade.[6] Similar regulation of apoptotic apical extrusion involving actomyosin contractility by S1P and RhoA have been observed in cultured epithelial cell lines[5,7]

Oscillations in the shape of apoptotic extruding cells raise several questions concerning the mechanical agency of extruding cells and the dependence of extrusion on the microenvironment. What is the role of the local mechanical environment in promoting extrusion? Epithelial cell behaviors are commonly regulated and constrained by their neighbors. Are the pulsatile contractions coordinated between cells? Epithelial cells in many embryos and larvae exhibit area oscillations, but it is unknown if these oscillations are adaptive. Does a cell facilitate its own exit or is it pushed? Extrusion involves dynamic changes in cell adhesion and contractility in both the extruding cell and its neighbors, but we know little about the relative mechanical contributions of these cell biological changes. To address these questions, we divide our interest in the biophysics of extrusion into two categories, first, considering processes operating in the extruding cell (e.g., autonomous mechanical processes), and second, processes modulating extrusion that operate within cells in contact with the extruding cell (non-autonomous mechanical processes). Akin to intrinsic properties, autonomous mechanics refers to the biophysical properties of the extruding cell that influence the kinematics of extrusion, including steady state mechanical properties as well as the strength, rate, and periodicity of cyclic contractility. Conversely non-autonomous processes refer to properties of the extruding cell's microenvironment such as the neighboring cells' mechanical properties and cyclic contractility, and tissue confinement. While optogenetic tools are beginning to be used to modulate cell and tissue level forces,[8] it is currently not possible to predictably manipulate biophysical properties such as amplitude or frequency of cell area strains. To

[1]Department of Bioengineering, University of Pittsburgh, Pittsburgh, PA 15260, USA
[2]Computational Modeling and Simulation Graduate Program, University of Pittsburgh, Pittsburgh, PA 15260, USA
[3]Department of Genetics, University of Texas MD Anderson Cancer Center, Houston, TX 77030, USA
[4]Genetics and Epigenetics Graduate Program, University of Texas MD Anderson Cancer Center UTHealth Houston Graduate School of Biomedical Sciences, Houston, TX 77030, USA
[5]Department of Developmental Biology, University of Pittsburgh, Pittsburgh, PA 15260, USA
[6]Department of Computational and Systems Biology, University of Pittsburgh, Pittsburgh, PA 15260, USA
[7]Lead contact
*Correspondence: gteisenhoffer@mdanderson.org (G.T.E.), lad43@pitt.edu (L.A.D.)
https://doi.org/10.1016/j.isci.2024.111017

address these outstanding questions, we sought to build a computational model where the roles of cell-autonomous and non-cell-autonomous mechanics in driving apical extrusion could be tested and compared quantitatively.

Epithelial homeostasis and morphogenesis have been simulated in several different frameworks, each with their own assumptions and implementation techniques.[9,10] The most simple physical analog of extrusion is the T2 transition within soap film arrays (e.g., wet foams), where cell loss occurs through a 3-neighbor cell array that computational models of epithelia try to capture.[11] Vertex models are the most common biophysical models of epithelia.[12] In vertex models, the dynamics of apical epithelial vertex movements minimize area and perimeter deviations from preferred values amidst dynamic force imbalances between the medioapical cell cortex and apical cell-cell junctions.[13–20] A Cellular Potts Model can also facilitate simulation of epithelial cell dynamics, where packets of cytoplasm are distributed among cells in an epithelium to minimize an energy functional representing apical and junctional elastic energy.[21–24] These models are less suited to oscillations in cell areas and would require very fine and computationally expensive discretization to do so. Finite element models have also been used to represent epithelial tissue-scale dynamics.[25–28] Given how cells are partitioned in these models, the same challenges for implementing oscillations in cell area as Cellular Potts models remain. Agent-based, or active particle models represent epithelial cells, or their centers, as particles that can be endowed with biophysical properties and rules governing their interactions.[29] Cell junctions composing an epithelial sheet in an active particle model can be represented by tiling or tessellating a set of cell centers.[30,31] Another type of model is the phase-field model which specializes in the moving boundary problem within the phase field denoting cell locations.[32,33] Cell boundaries involve changes in said phase field defined in terms of partial differential equations (PDEs). These are somewhat more suited to representing area oscillations but require more complex definitions of the PDEs involved. Each of these simulation frameworks can represent discrete cells and enable direct quantitative comparison with experiments depending on the choice of analysis techniques. We prioritize model parsimony and a limited parameter set for representing area oscillations during extruding processes. We chose an active particle model to allow centroid-focused control over cellular responses rather than defining these changes in terms of cytoplasmic packets or individual cell vertices. Moreover, mechanical responses and initial conditions in these models are typically more intuitive and lend to more ease of interpretability. This primes our model for later sensitivity analyses by limiting factors that might confound our results and require possible non-dimensionalization.

Within our active particle model, we need to designate a potential consistent with other cell-center models. Center-based active particles models are often formulated with cells repelling one another when spaced more closely than their interaction distance, which is typically in terms of a single cell diameter.[34] How do we maintain tissue cohesivity without a pairwise attraction? We find that having cells interacting within one cell diameter of each other in a dense regime with fixed borders allows them to be tesselated into an epithelial sheet with movements that mimic live cells (Figures 1 and S3). Repulsion range can be represented with a Gaussian function,[35] but this diminishes elasticity for more dense packing. We use an elastic function for this repulsion in a linear fashion, as done in vertex models. Other models have included viscous elements,[36] but our simulation parameters with initial potential and resting length can be more precisely controlled with an elastic descriptor. This descriptor accounts for dissipation due to both friction and adhesion forces. This is somewhat analogous to vertex model repulsive potentials if one considers connecting cell centroids with springs rather than vertices. The key difference here is that our model does not have a closed-form energetic description, as we take a cell-by-cell force-based approach, in line with other cell-center models[37] that use tessellation to render these centroids into the confluent sheet topology characteristic of epithelia.[38]

It is not common to see extrusion simulated explicitly or quantified in the aforementioned modeling frameworks. A vertex model of delamination from an overcrowded tissue[39] incorporated triangular cells with small areas that can be removed. Vertex models have also been used to interrogate parameters needed to form a rosette characteristic of the extrusion process through significant increases of extruding cell contractility and local adhesions.[40] Use of a vertex model in three dimensions (3D) sought to establish mechanical instability and symmetry breaking as a precursor to cell extrusion on both the apical basal sides as a function of cell density and forces.[41] A 3D phase field model of extrusion was applied to focus on cell-cell and cell-substrate interactions with an emphasis on adhesion forces, underscoring the role localized stress.[42] Additionally, combining phase field and vertex modeling approaches have been applied to represent extrusion to focus on gastric cancer and ECM attachment.[43] There is a need for a model in which the dynamics of extrusion is parameterized and manipulable to independently test the roles of cell-autonomous and non-cell-autonomous drivers. We sought to reduce model complexity to the 2D space, as we are studying the mechanics contributing to apical extrusion and have intuitive parameters acting on a cell-to-cell basis for precise manipulations *in silico*. Of the various modeling frameworks, active particle models can be developed with minimal sets of parameters and implemented with a limited set of assumptions on cell adhesions and intracellular remodeling.[44] Active particle models have not been previously used to interrogate extrusion. As of yet, no computational models have sought to isolate the contribution of the local mechanical microenvironment in oscillations of cell area that contribute to extrusion.

To explore the biophysical principles regulating cells extrusion in the larval zebrafish, we developed an active particle model that represents the dynamic and stochastic mechanics of the extruding cell and its surroundings. Such a model needed to account for several experimental observations including a sudden drop in area upon the onset of extrusion, and rachet-like oscillatory decreases in area in the extruding cell with a range of amplitudes and periods. While active particle models have been useful in the analysis of epithelial morphogenesis and solidto fluid-like transitions that allow jammed tissues to flow, these models have not previously been used to investigate extrusion. Initially, we sought to represent apical cell junctions by tiling cell centers via Voronoi tessellation. However, we found such tessellation schemes could not represent mechanically heterogeneous cell populations, but only the geometry of cell positions.[45–47] To properly represent both the mechanical and geometrical heterogeneity of cells in a 2D sheet, we developed a hybrid tessellation that integrated mechanical interactions within the centroidal Voronoi Tessellation framework (hybrid CVT). This hybrid tessellation framework allowed extruding cells to
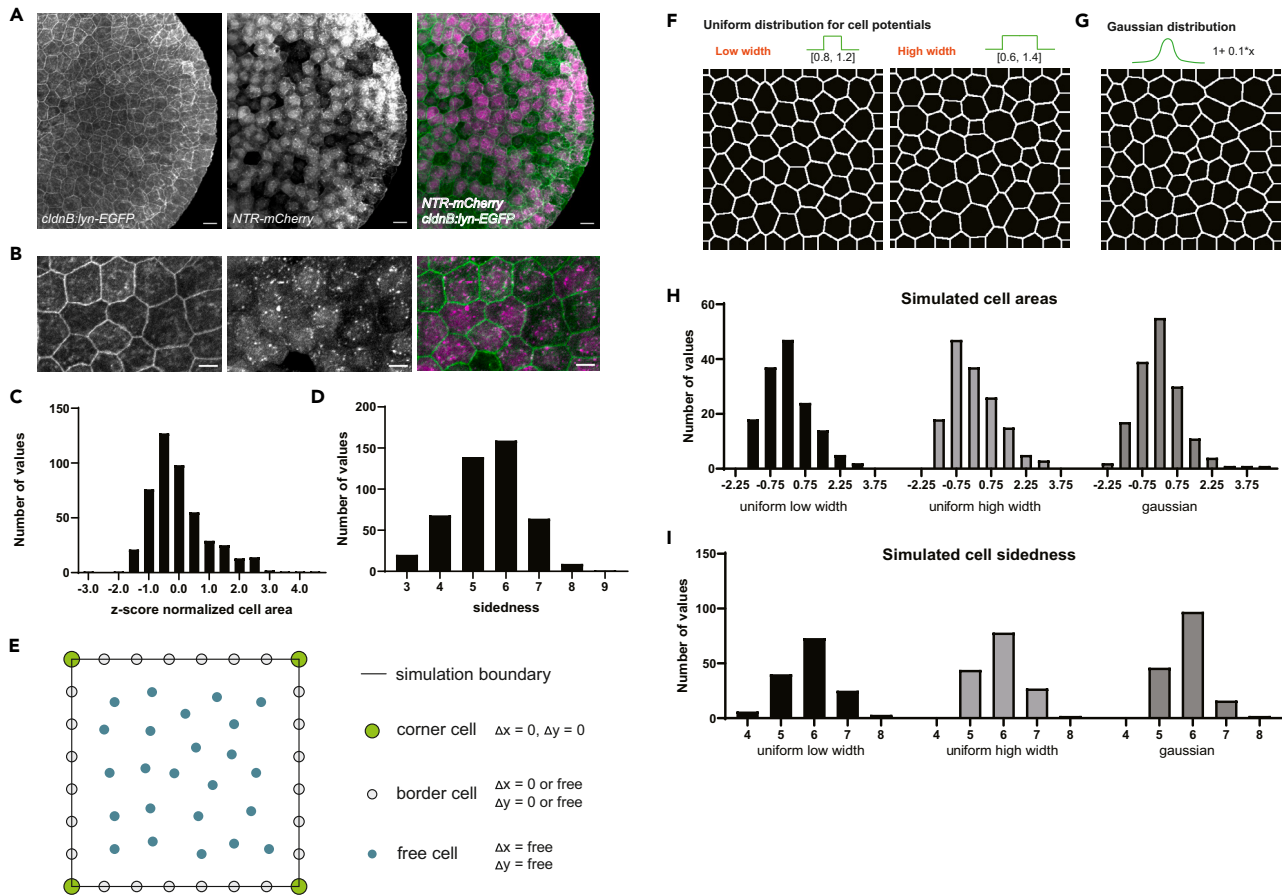
Figure 1. *In vivo* and *in-silico* epithelium at equilibrium, also see Figures S1, S3 and S10

(A) The larval zebrafish tail fin epithelium with cell-cell junctions fluorescently labeled. (Scale bar = 20μm).

(B) Close up of larval zebrafish epithelium with the expression of NTR-mCherry (Scale bar = 10μm).

(C) *Z* score normalized distribution of areas of tailbud epithelium cells.

(D) Sidedness distribution of tailbud epithelium cells (*n* = 10 larvae, 464 total cells).

(E) Schematic of types of cells in simulation and their movement restrictions.

(F) Cell fields obtained from using low and high width uniform distributions for sampling cell size.

(G) Cell fields obtained from using a Gaussian distribution for sampling cell size.

(H) *Z* score normalized cell area distributions for the three distributions over 10 simulations each (*n* = 141,151,161).

(I) Cell sidedness distributions for the three distributions over 10 simulations each (*n* = 141,151,161).

be represented with small areas and mechanically driven oscillations. We simulate mechanical interactions through repulsive cell potentials and incorporate these potentials to map cell-cell boundaries of extruding cells and their neighbors. In addition to providing control over cell-to-cell biophysical properties, the model allows us to test the effect of tissue-wide properties such as viscosity and cell packing on extrusion. By testing each of these features, we have been able to quantify the role of extruding cell autonomy and demonstrate that nonautonomous factors may play a smaller role than earlier suggested.

RESULTS

Topology of the zebrafish larval epidermis

To better understand variation of the size and shape of cells within the zebrafish larval epidermis, we first determined the polygon distribution of cells within the epithelium under homeostatic conditions and captured how these parameters could fluctuate from larvae to larvae. Confocal images of the tail fin epithelium of transgenic larvae were collected 4 days post-fertilization (dpf) were collected using fluorescent proteins that localize to epithelial cell-cell junctions (cldnBlyn-GFP) and NTR as part of the inducible apoptotic system (NTR-mCherry) (Figure 1A, Video S1). We confirmed the expression of with a closer look at the larval zebrafish tail fin (Figure 1B). Morphometric analysis showed over 55.7% of cells in the epithelium have an area of 800–1000μm² in a skewed-right distribution (Figure 1C), and are comprised of 29.9% pentagons, 34.2% hexagons, 13.8% heptagons, 1.9% octagons, and 0.2% nonagons (Figure 1D). These data are consistent with the observed polygon topology of the epidermis in other eukaryotes, including the epidermis of the *Xenopus* tadpole tail, the outer epidermis of the

freshwater cnidarian *Hydra,* the *Drosophila* wing disc epithelia, and the epidermis of plants.[48] In all of these cases, a similar non-gaussian distribution of epithelial polygons is observed with less than 50% hexagonal cells and high percentages of pentagonal and heptagonal cells. These data support the idea that similar topological distributions are present in other multicellular eukaryotes and provide the basis for a ground state for a computational model of epithelial dynamics.

Active particle representation of a mechanically and geometrically heterogeneous epithelium

To simulate an epithelial sheet of cells, we developed a lattice-free model where cells are represented by interacting particles, or nodes, that are positioned within a two-dimensional rectangular domain. Cells in this rectangular patch are represented by three types of nodes: (1) corner nodes represent quarter-cells that connect the four corners of tissue to the domain boundary, (2) border nodes represent half-cells that connect the four tissue edges to the domain boundary, and (3) interior free nodes represent full sized cells in the epithelium within the domain. Corner nodes do not move, whereas border nodes are free to move along the axes that demarcate the domain boundary. Interior nodes may move freely within the 2D domain. Border and internal nodes move as they interact with each other and move toward mechanical equilibrium via repulsion forces operating between all nodes (Figure 1E). Node movements are governed by a force balance enforcing Langevin dynamics, incorporating stochasticity and drag forces from viscous media.[49] We represent the mechanical elasticity of each cell with a non-linear repulsive spring. Each cell is a node with its own unique mechanical properties. We represent the mechanical heterogeneity of the epithelium by assigning each node a repulsive potential that is randomly selected from a uniformly distributed set of potentials/rest lengths ($rest_{i,j,k}$ ...). Forces act within an interaction distance, *rest,* of cell *i* (Equation 1),

$$rest = \frac{diameter\left(rest_i + rest_j\right)}{2} \qquad \text{(Equation 1)}$$

where *diameter* is an average cell diameter and $rest_i$ and $rest_j$ are rest lengths of cell *i* and other cells *j*. These rest lengths determine repulsion forces between two cells as a function of diameter and the distance between them (Equation 2),

$$F_x = \frac{dist - rest}{rest} * \frac{dx}{dist} \; ; \; F_y = \frac{dist - rest}{rest} * \frac{dy}{dist} \qquad \text{(Equation 2)}$$

where the distance, *dist*, is calculated between adjacent nodes and resolved into its components *dx* and *dy* and used to calculate forces in the x and y directions, F_x and F_y, respectively. Force is calculated in the x and y directions between cell i and cells j at a distance less than *rest* away. The x and y forces are summed for all cells within the interaction distance (Equation 3),

$$F_{x,total} = \sum_{i}^{j} F_x; F_{y,total} = \sum_{i}^{j} F_y \qquad \text{(Equation 3)}$$

Cell motion occurs as force is scaled by viscosity and the simulation is advanced in time using forward Euler methods (Equation 4),

$$x_{i,t} = x_{i,t-1} + \mu * F_{x,total} * \Delta t \; ; \; y_{i,t} = y_{i,t-1} + \mu * F_{y,total} * \Delta t \qquad \text{(Equation 4)}$$

where each x and y position at a given time *t*, $x_{i,t}$ and $y_{i,t}$, are calculated using the position in the previous time *t-1* and the calculated total force. Viscosity is represented by μ and change in time between *t* and *t-1* is *Δt*. The viscosity term is multiplied and not divided by force. Thus, higher viscosity values indicate lower viscosity, or lower resistance to flow.

To visualize changes in epithelial cell morphology and network topology, we convert our array of nodes into a 2D graph of topologically connected cells with defined shapes and areas. One option for conversion is a Voronoi tessellation of the centroids. Voronoi tessellations are commonly used to mimic epithelial shape distributions in active particle models.[31,38,50,51] These tessellations have known limitations, particularly in representing cell shape asymmetries and heterogeneity present in tissues responding to anisotropic forces.[52] A shortcoming of using the Voronoi tessellation with our study is that it cannot represent sufficiently small cells, even if cell centroids become close to each other (Figure S2). One alternative is to use the centroidal Voronoi tessellation (CVT) to form the 2D graph; CVT determines the centroid of each triangle in a Delaunay triangulation and connects them with straight lines. However, this method is also purely geometric, like the Voronoi tessellation, and is similarly limited in representing the cell size heterogeneity present in our model system. We developed a method to reflect the heterogeneity of geometric organization and arrangement of cell sizes observed *in vivo*. Like the CVT method, we first calculate the circumcenters of the triangle but then shift their positions by the weighted centroid of the potentials of the nearby cells, leveraging the physics of the system. We average the weighted centers with the original Voronoi circumcenters and connect them, creating our own hybrid CVT (Figure S2). To extract cell areas, we perform a segmentation. It is important to note that the potential function of the cell does not directly correlate with the measured area. There is a not a closed form representation linking cell potentials to areas, as is done in some other modeling frameworks. The potential function drives cell centroid movement, which is affected by the potentials of neighboring cells and tissue-wide properties. These centroids are then tessellated using the described hybrid CVT strategy. The cells visualized through this process are the subject of our analyses. Taken together, our model, tessellation scheme, and analysis pipeline (Figure S1) provide us a framework in which we can recapitulate extrusion events in the tail fin epithelium of larval zebrafish.

Cell heterogeneity as captured by simulation

As there is variation in cell morphology from embryo to embryo, as well as across the same tissue, we developed our model to represent this variability. To generate diverse cell areas and sidedness in the epithelium at rest, we sample individual cell rest lengths from three distributions of rest lengths, including two uniform distributions (Figure 1F) and an adjusted Gaussian distribution (Figure 1G) centered at 1.0. Preliminary analysis indicated that tissue packing also affects area and sidedness, with lower packing yielding more varied area and sidedness, so we chose distributions that result in lower levels of packing (Figure S3). The area and sidedness across the three cases are not significantly different from each other ($p > 0.05$; two-sample Kolmogorov-Smirnov test). Furthermore, area distributions are not significantly different from the area measurements from cells in living epithelia (Figures 1C and 1D), however, sidedness in the simulations differs from these *in vivo* data (Figures 1H and 1I). To offset this difference, we chose to sample cell potentials from the uniform high width distribution as it yielded a lower sum of test statistics compared to the live cell area and sidedness (Table S1).

Cell potential oscillations generate kinematic changes in apical surface area and can be used to drive extrusion

In the larval zebrafish epithelium, cell areas vary in two distinct modes, decreasingly sinusoidal in extruding cells, and sinusoidally in neighboring cells (Figures 2A–2C). We use cell area strain to compare changes in area over time ($area_{final}$, $area_{initial}$) to account for cell area variation:

$$area\ strain\ =\ \frac{area_{final}\ -\ area_{intial}}{area_{intial}} \qquad \text{(Equation 5)}$$

In order to drive cell area oscillation as seen *in vivo*, we apply a time-varying sinusoidal potential, $rest_i$, to a cell (Equation 6),

$$rest_i(t)\ =\ a_i * sin(b_i * t + c_i) + start_i \qquad \text{(Equation 6)}$$

where *a* represents the oscillation amplitude, *b* represents the frequency, and *c* represents the phase of the oscillation. There are multiple periodic functions that could be used to describe a driving function of simulated extruding cells. We tested three candidate functions: a sinusoid, sawtooth, and a square wave (Figure S4A). These were put in a linearly decreasing form (Figure S4B). Representative cell area strains are shown for the square wave function (Figure S4C) and the sawtooth function. While these captured the decreasing area strains, we used the Mann Whitney U test to compare amplitudes extracted using the Hilbert envelope (Figure S6) to live cells ($n = 14$ live cells, $n = 15$ simulated cells for each case, with 200+ extracted amplitudes total). For the sawtooth function, the amplitudes were significantly different ($p < 0.05$). For the square wave, the amplitudes match those from the live cells ($p = 0.13$). The case best matching the live cells was the sinusoidal case ($p = 0.23$, Figure 2D). Thus, we used the sinusoidal function for our simulations. (Figure S4).

The observed variations in cell areas within the larval zebrafish epidermis (Figures 1C, 2C, and 2E) may reflect cell-intrinsic mechanical differences. To represent this variation, we assign different rest potentials to individual cells ($start_i$, $start_j$, $start_k$). However, cell area fluctuation, or oscillation, is a common feature of animal epithelia, and *in vivo* observations of MTZ-treated tail epidermis reveal apical area oscillations during the process of cell elimination by extrusion. Therefore, oscillation through the sinusoidal term was added to the start potential (Equation 6). Two cells can oscillate in-phase, where high levels of potential are synchronized ($c_i = c_j = 0$ for both cells) or can oscillate out of phase ($c_i - c_j \neq 0°$). In our model system, cell areas oscillate out of phase (Figures 2C–2E). To make the oscillation cause cell area to decrease over time, we included a linear term with slope d_i (Equation 7),

$$rest_i(t)\ =\ a_i * sin(b_i * t + c_i) - d_i * t + start_i \qquad \text{(Equation 7)}$$

By implementing these equations, we can represent cell area changes seen *in vivo* during extrusion. Despite not defining stable oscillations in the extruding cell potential function, we see this emerge in the area strains of some extruding cells (Figure 2D). We also see increasing amplitudes of area strain despite the potential function having constant amplitude. Another emergent property is that cell area strains can oscillate out of phase with the driving potential, exhibiting the phase variation observed *in vivo* (Figure 2E). Thus, variations in cell area, and the dynamics of apical areas during extrusion can be represented by the described time-varying rest potential.

To quantify how changing the model parameters affects area strain in simulated extruding cells, we calculate the time to half area loss (t_{half}) and the slope when the time to half area loss is reached ($slope_{half}$; Figure 2F). We interpolate these quantities between peaks where absolute half area loss is reached to minimize dependence on amplitude and frequency of the driving potential. While these do not have a 1:1 correlation with cell area, we wanted to decrease their bias on output data. Other endpoints such as local strain and strain along the x and y directions were considered but were not as varied across simulations (Figure S9).

Base extrusion model: A minimal model of extrusion of an oscillating cell

Cell shape oscillation can be driven by varying the cell's potential function over time. As individual cells are extruded apically after MTZ treatment, they exhibit a distinctive form of oscillation. The cell starts with an initial area that oscillates, and then the cell loses a large portion of its area (Figure 2C and Equation 7). Additionally, epidermal cells immediately adjacent to extruding cells also exhibit distinctive, high amplitude oscillations, also driven by a time-varying potential (Equation 6). While multiple cells can be made to extrude in a single simulation, we chose to have only one cell leave at a time to avoid confounding effects of distant oscillations (Figure S10, Video S2).

Using this approach, we sought to simulate key observations of extruding cells in living epithelia including oscillatory area changes with the magnitude observed *in vivo*. There is a key distinction to be made with regard to the initial phases of extrusion observed of cells in living tissues (Figure 2C). There are area oscillations that appear to be stable but transient before rapid area loss is achieved. Cells are imaged
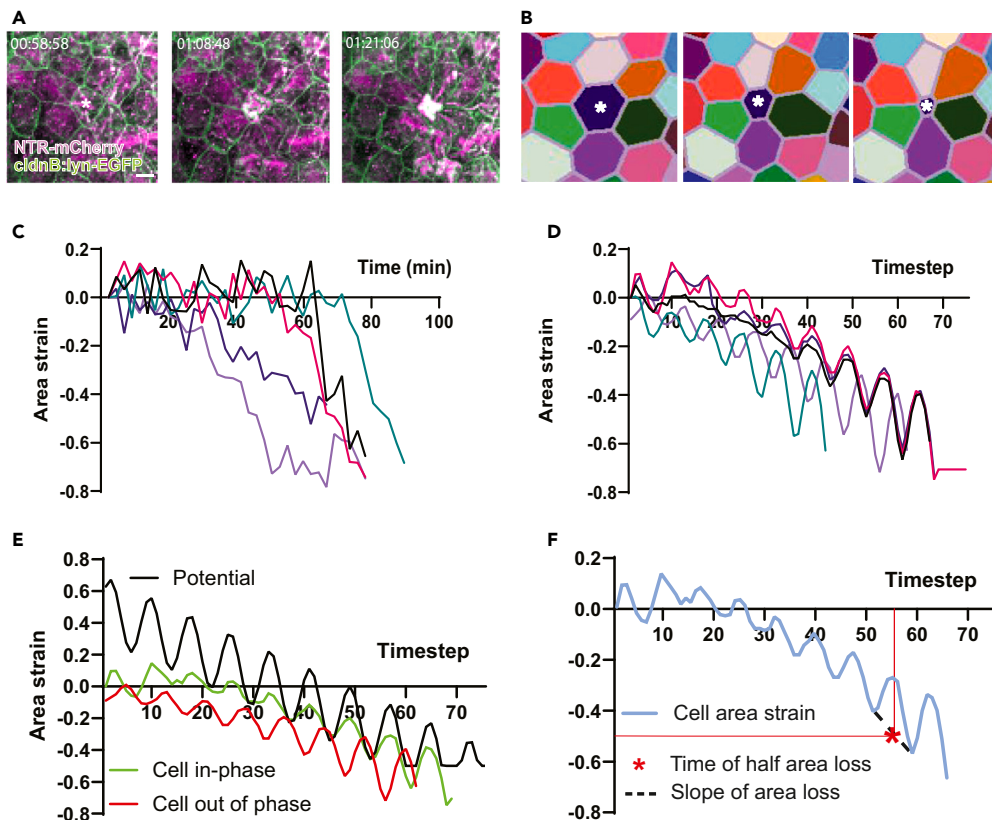
Figure 2. Quantifying and modeling epithelial cell extrusion, also see Figures S2, S5, S6, S9; Table S1

(A) Time-lapse imaging of cells extruding from the larval zebrafish epidermis.

(B) A simulated extruding cell over time.

(C) Five representative area strain trajectories of extruding cells from time-lapse imaging data.

(D) Five simulated cell area trajectories matching cell trajectories.

(E) Potential function with a sample initial potential of 0.62 and the base parameters and two cell area strain trajectories of different phase.

(F) Extraction of our output metrics of time to half area loss and slope of area loss from a cell area strain trajectory.

at various times of their extrusion processes, with some having longer periods of stable oscillations than others. We want to start all simulated cells at the point at which rapid area loss begins, so we do not include a period of stable oscillation in potential in our simulations. We are simulating variations in extrusion phenotypes, not the triggering of the process itself; however, we do see stable oscillations in some cells despite their potentials already decreasing. To accommodate this range of features, we varied parameters of the driving potential to mimic changes of experimentally measured cell areas. We ran simulations with different parameters and compared the extruding cell's area trajectory to cell area trajectories observed in living epithelia. We compared the amplitudes of the extruding cells' area trajectories between the *in vivo* and *in silico* cases, showing that they are significantly similar (Mann Whitney U, $p > 0.05$, $n = 14$ live cells, $n = 15$ simulated cells, 200+ amplitudes in each case). We selected a set of parameters that generated extrusion over several simulations matching cell data observed *in vivo* (Table 1). This parameter set represents a base case for the perturbations to follow.

Model parameters can be varied to assess their effect on t_{half} and $slope_{half}$ (Figure 3). Within the cell autonomous regime, we can vary properties of the extruding cell potential, such as amplitude (*a*), frequency (*b*), and initial rest length (*start*). We also considered changing the slope of the extruding cell potential, but keeping it constant helped isolate other factors contributing to the rate of extrusion (Figure S7). Beyond the extruding cell, we consider two nonautonomous contributors: the microenvironment and the macroenvironment. We can assess the effect of the microenvironment on extrusion by changing the neighbor cell potential function's amplitude (*a*), frequency (*b*), and initial rest length (*start*). We can assess the role of the macroenvironment on extrusion by changing viscosity (*μ*) and packing (*p*).

Extruding cell potential is a key source of variation in extrusion timing

To explore the role of cell autonomous factors on extrusion, we varied properties of the extruding cell and measured how these parameters contribute to the dynamics of extrusion while maintaining the geometry and mechanical properties of neighboring cells. First, we vary the amplitude and the frequency. Ranges are chosen to capture physiologically observed variation. Multiple simulations are run with specifically

Table 1. This is the set of parameters used for the base case

Parameter	Value
Amplitude	0.2
Frequency	0.8
Slope	0.014
Packing	0.9
Viscosity	15
Amplitude neighbors	0.2
Frequency neighbors	0.8
Distribution used for rest length	Uniform
Minimum of distribution	0.6
Width of distribution	0.8

varied parameter sets. Each simulation generates a single-cell extrusion event over a time series where cell centers are tessellated to produce an epithelial array. Characteristic extrusion features t_{half} and the $slope_{half}$ are extracted from the extruding cell area changes during extrusion (Figure 2F). For the same initial potential, we observe differences in t_{half} as amplitude changes (Figure 4A, Videos S3 and S4) but do not observe changes in the $slope_{half}$ (Figures 4B and S8A). By varying the frequency of oscillation, we do not observe differences in t_{half} (Figure 4C, Videos S5 and S6). However, unlike when we changed amplitude, variation in the frequency of oscillation alters $slope_{half}$, especially at high and low frequencies (Figures 4D and S8B).

The initial mechanical state or size of a cell may contribute to the dynamics of extrusion. We tested this possibility by using a range of initial potentials for extruding cells using the bounds of the selected uniform distribution to capture the full range of initial cell sizes possible. The potential of a cell is a major contributor to its size before extrusion (Figure 1G). Additional contributions to a cell's size are the potentials of its immediate neighbors and global packing within the tissue. From these simulations we find a positive correlation between the initial potential of a cell and the cell's t_{half} ($R^2 = 0.8587$) (Figures 4E and S8C). Furthermore, $slope_{half}$ has a mild positive correlation with the initial potential of the extruding cell ($R^2 = 0.18$) (Figure 4F), indicating cells that are large due to their low potential are also slower to extrude. Observations in zebrafish suggest that larger cells might extrude more slowly than smaller cells[6] (Figure S5).

Cell potentials of neighboring cells and the local mechanical environment can play a role in extrusion timing

Next, we query the contribution of nonautonomous biophysical factors on extrusion dynamics. To isolate the contribution of the mechanical environment of the extruding cell, we hold constant the potential function of the extruding cell and vary the potential of neighbor cells. While the neighbor cell potentials do not experience a linear decrease like extruding cells, they do experience oscillations (Figure 3). Based on our live cell observations, the neighbor cell areas oscillate out of phase with each other, so the beginning of each neighbor cells' oscillations is randomized in the first ten timesteps of the simulation. The neighbor cells' potential oscillations are set up to vary in a similar way: increasing and decreasing each parameter from their baseline levels of amplitude and frequency. After varying amplitude, we find the amplitude of neighbor cell oscillation has a minimal effect on extruding cell area loss (Figures 5A, 5B, Videos S7, and S8E). When neighboring cells pulse with a higher amplitude, there are stronger oscillations in the extruding cell, indicating more mechanical resistance. The most mechanical resistance occurs for the highest neighbor oscillatory amplitude and the lack of a stable phase in the case of the lowest neighbor oscillatory amplitude. After varying period, we find little effect on t_{half} and $slope_{half}$ (Figures 5C, 5D, Videos S8, and S8F).

After varying the properties of extruding cells or their neighbors, we turned to varying the bulk mechanical properties of the tissue, or macroenvironment, particularly density and viscosity. The mechanical status of a tissue may act through mechanobiological feedback to influence the assembly of contractile structures within the cell[53,54]; however, we do not explicitly include such feedback processes in our model and still see a profound impact. Viscosity may contribute to extrusion phenotypes due to dampening the effect of forces from contractility-driven oscillations within the tissue.[55,56] Changing the viscosity modifies the timescale with which the tissue responds or deforms after an applied force. If contractions from oscillations propagate through the tissue more slowly, this may affect the t_{half} and $slope_{half}$. Changing levels of viscosity have an effect on t_{half} and no effect on the $slope_{half}$ (Figures 5E, 5F, and S8H). It appears that less viscous tissues slow down the time to half area loss. Another factor impacting the micromechanical environment of the tissue is how cells are confined or distributed in space, which in turn affects tissue mechanics. Crowding is known to induce extrusion of non-apoptotic (live) cells[3]; therefore, we tested the effect of packing density on extrusion dynamics. We predicted that higher cell density will make cells extrude faster due to having lower areas, similar to the case of low rest lengths (Figure 4E). We find agreement with this prediction, and observe that higher levels of packing drives cells to extrude in less time, albeit at a similar rate (Figures 5G, 5H, S5, and S8G). Another readout of the role of the mechanical environment is the strain response when extruding cells have identical potential functions, including the initial rest length. Our analysis (Figure S8D) indicates that cell areas can indeed vary in this case and that there is a role for variation due to nonautonomous mechanics. We next sought to methodically determine the sources of this variation.
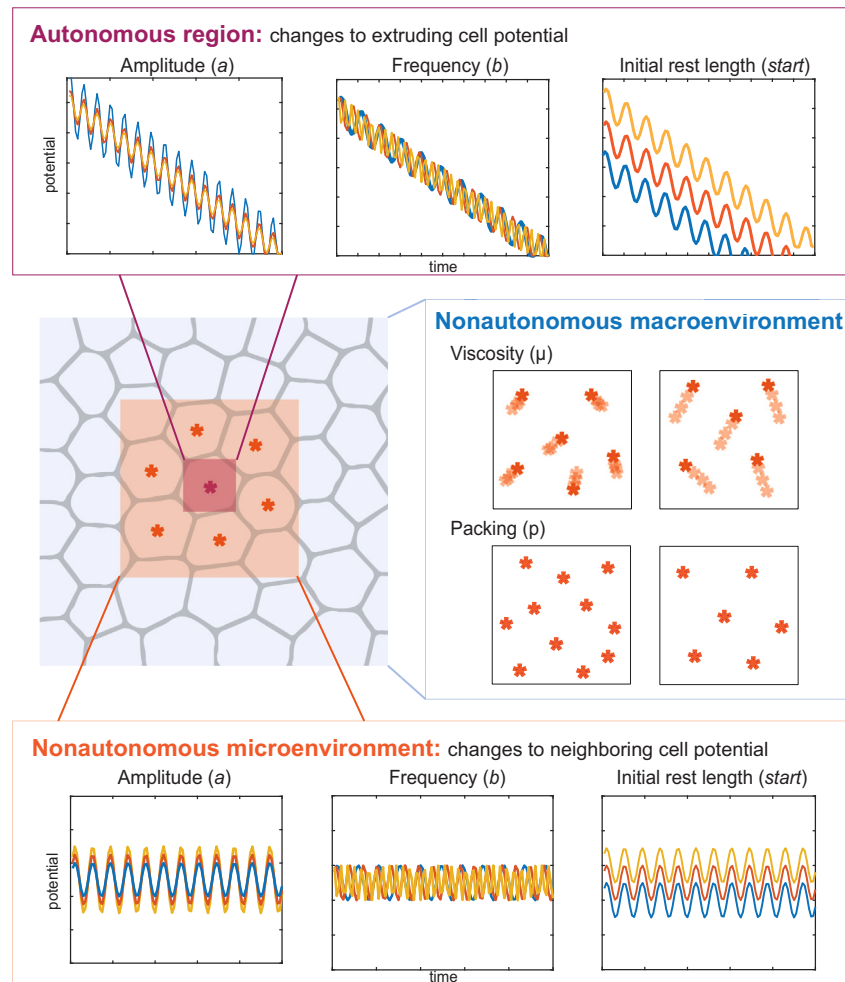
Figure 3. Key parameters used for assessing cell autonomy

Across three scales, the autonomous region, nonautonomous microenvironment, and the nonautonomous macroenvironment, there are eight parameters that are varied to assess their contributions to time to half area loss and the slope of area loss. Asterisks indicate cell centroids and the colors represent different scales, with red being the smallest autonomous scale, orange being the nonautonomous microenvironment, and blue being the nonautonomous macroenvironment.

Sources of variation in extruding cell area loss

Our model delineates the effects of cell behaviors and tissue mechanics on t_{half} and $slope_{half}$. Yet, due to the stochastic nature of cell behaviors across the field, we were not able to precisely control variation that may contribute to the duration of extrusion. To reduce bias from the contributions of stochastic factors and determine precise contributions of each parameter to variation in t_{half} and $slope_{half}$, we performed a sensitivity analysis. Previously, when assessing cell autonomous effectors of extrusion, the focus was on the initial mechanical state of the cell and features of its oscillatory resting potential (Figure 4). To determine how these features contribute to variation in outcomes, we sought to consider the initial rest length of the extruding cell and the amplitude and frequency of the rest length oscillation. As non-autonomous factors such as the neighbor cells and mechanical environment also contribute to extrusion (Figure 5), we sought to assess their relative contributions. For neighboring cells, we assessed the parallel features to extruding cells: initial rest length, amplitude, and frequency of oscillation. For the tissue mechanical environment, we again consider viscosity and packing, as they appeared to contribute to extrusion dynamics (Figures 5E–5H).

To define the ranges of the eight model parameters and make comparisons relative, we matched ranges for parameters of the extruding and the neighboring cells. We tested the contribution of a range of initial rest lengths to the geometric heterogeneity of the model epithelium (Figures 1F–1H). Given the impact of rest length on area and sidedness (Figures 1H and 1I) and the wide range of area and sidedness seen *in vivo* (Figures 1C and 1D), we selected cell potentials from the high-width uniform distribution. For the amplitudes and frequencies of the extruding cells and their neighbors, the same ranges/deviations from the base case were used. For determining the ranges of viscosity and packing in the model, direct literature comparisons were lacking, so we similarly chose values greater and lesser than that of the experimentally determined base case to capture variation. Simulations carried out at the bounds of parameter ranges were visually inspected for stability of the tessellation and segmentation.
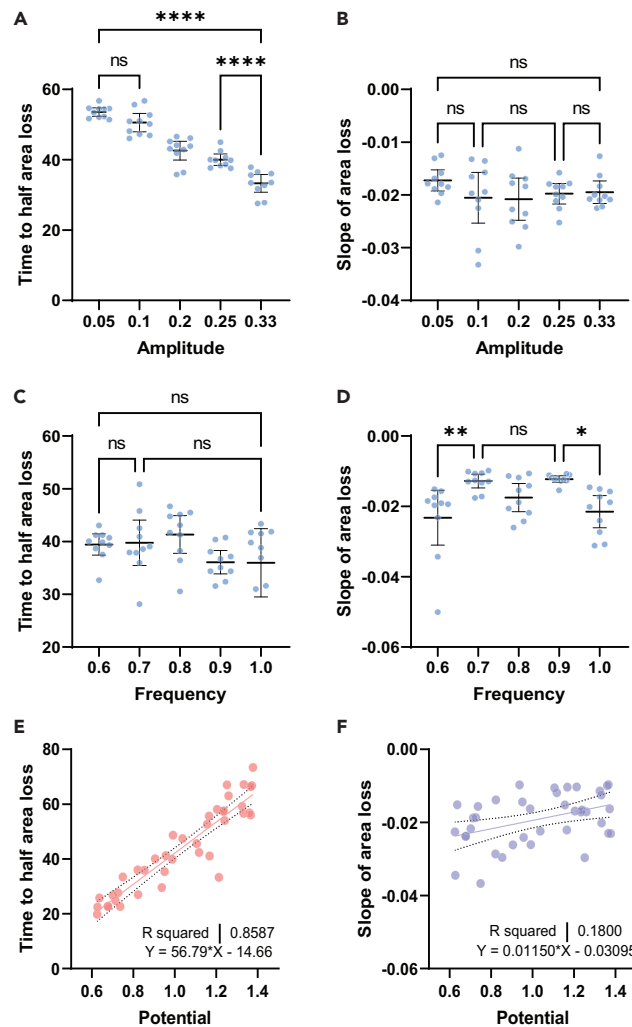
Figure 4. Effects of cell-autonomous properties on extrusion dynamics, also see Figures S4 and S5

(A) Effect of autonomous amplitude change on time on half area loss.

(B) Effect of autonomous amplitude change on slope of area loss.

(C) Effect of autonomous oscillatory period change on time on half area loss.

(D) Effect of autonomous oscillatory period change on slope of area loss.

(E) Initial rest length/potential of the extruding cell as a function of time to half area loss for $n = 40$ simulations.

(F) Slope of area loss related to initial potential of the extruding cell for the same 40 simulations. All data are represented as mean $\pm$ 95% confidence interval.

To assess parameter contributions to extrusion dynamics, we used extended Fourier Amplitude Sensitivity Testing.[57] To implement the eFAST technique, we sample input parameters from periodic distributions. Associated model outcomes and peaks thereof are used to calculate Sobol indices to quantify parameter contributions to time to half area loss and the slope of the area loss (t_{half} and $slope_{half}$). Two Sobol indices are calculated (Figure 6A): the first order index (S1) reports how sensitive the output is to a parameter's variation, with high values indicating more sensitivity. The total order index (ST) reports synergistic effects of any order. Confidence intervals of these indices are also provided (Table S2).

Model parameters with the greatest effect on t_{half} are the extruding cell's initial rest length, amplitude, frequency of the neighbor extruding cell potential oscillation, and tissue viscosity. For all of these, the total Sobol index exceeds S1, indicating high order interactions between multiple parameters affecting the outcome more than the parameter on its own. Neighbor cell potential features have a lower impact on synergistic effects. For $slope_{half}$, the parameters contributing to the most variance are the rest length of the extruding cell, the packing of the tissue, and viscosity. The S1 index is close among all parameters, with neighbor cells having slightly lower values for both indices. In Figure 4D, we see an effect of the extruding cell frequency on the slope, yet no effect is seen in Figure 5D for the neighbor cell frequency. Our sensitivity analysis indicates that the two have the same contribution to variation in the slope of area loss; however, the extruding cell has a greater total synergistic contribution to this variation. The difference in discrete and continuous sensitivity analysis highlights the biological complexities
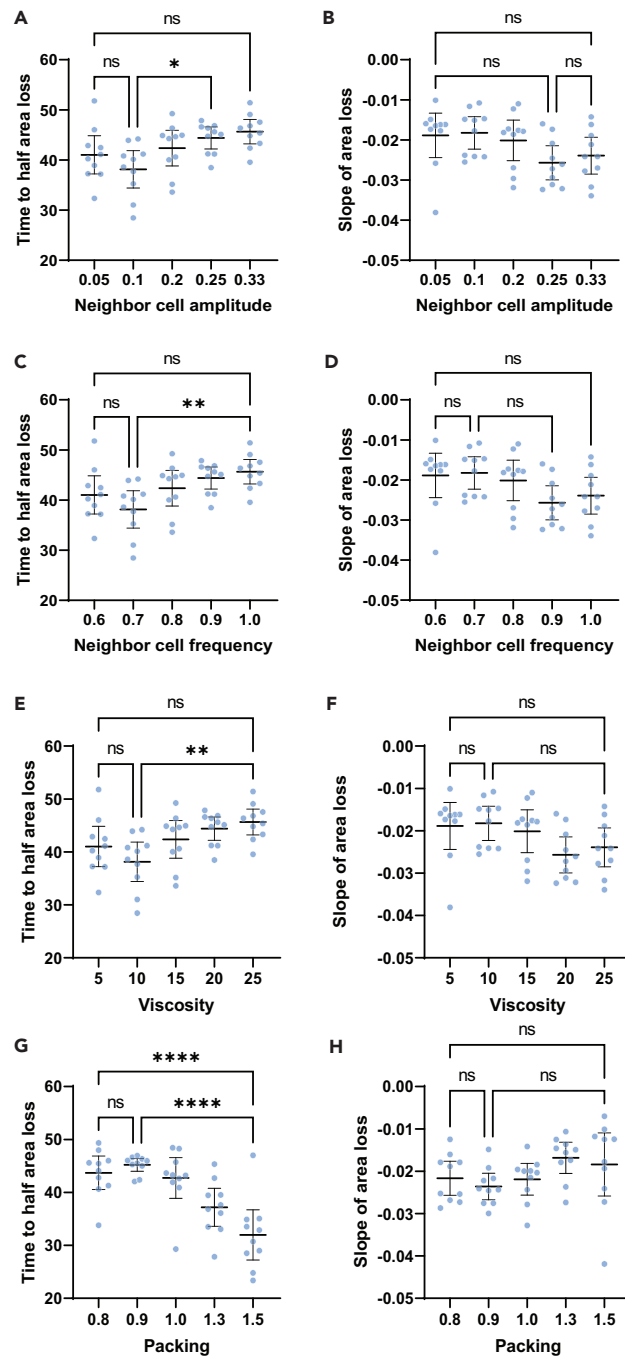
Figure 5. Non autonomous effects from cell neighbor and tissue-scale mechanics, also see Figure S5

(A) Effect of neighbor cell amplitude potential variation on time to half area loss.

(B) Effect of neighbor cell amplitude potential variation on slope of area loss.

(C) Effect of neighbor cell period potential variation on time to half area loss.

(D) Effect of neighbor cell period potential variation on slope of area loss.

(E) Effect of viscosity on time to half area loss.

(F) Effect of viscosity on slope of area loss.

(G) Effect of packing on time to half area loss.

(H) Effect of packing on slope of area loss. All data are represented as mean $\pm$ 95% confidence interval and each parameter group is averaged over 10 simulations.

A

Parameter	Range	S1 index for time to half area loss	ST index for time to half area loss	S1 index for slope of area loss	ST index for slope of area loss
Rest length	[0.6, 1.4]	0.34	0.71	0.16	0.91
Amplitude	[0.05, 0.33]	0.13	0.81	0.13	0.90
Frequency	[0.6, 1.0]	0.07	0.74	0.15	0.89
Rest length neighbors	[0.6, 1.4]	0.06	0.58	0.11	0.92
Amplitude neighbors	[0.05, 0.33]	0.10	0.53	0.12	0.78
Frequency neighbors	[0.6, 1.0]	0.14	0.92	0.15	0.80
Packing	[0.8, 1.5]	0.12	0.49	0.16	0.70
Viscosity	[5, 25]	0.14	0.41	0.17	0.83

B

Parameters affecting time to half area loss

SENSITIVITY: High, Med, Low

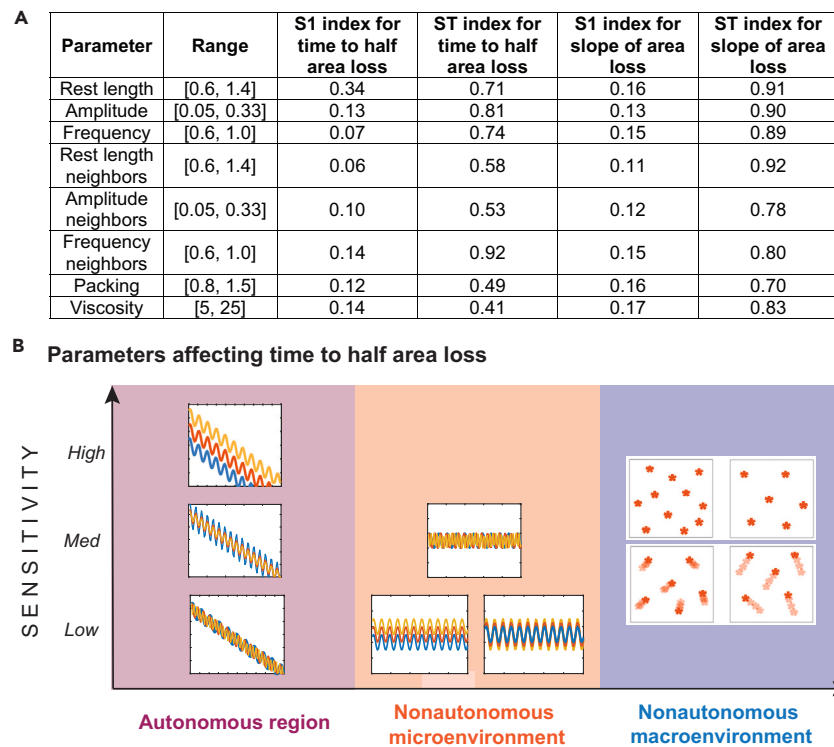**Autonomous region** — **Nonautonomous microenvironment** — **Nonautonomous macroenvironment**

Figure 6. Summary of contributors to extrusion dynamics, also see Table S2

(A) Table with parameter ranges for sensitivity analysis, with first (S1) and total (ST) order indices for time to half area loss and slope of area loss.

(B) Parameters affecting time to half area loss sorted by scale and level of contribution by S1 Sobol index (low = 0–0.1, med = 0.1–0.3, high = 0.3+). Colors of text in table correspond to different scales introduced in Figure 3, with the autonomous region being the smallest in red, nonautonomous micro- and macro-environments in orange and blue, respectively.

that our simple model is able to represent. This, in the context of our other results, indicates that smaller cells that are pulsing more strongly, with faster pulsing neighbors, moving more quickly, and are more confined in the tissue will extrude sooner. By binning the S1 Sobol indices across scales, we are able to gain insight into the role of individual parameters on the entire process of extrusion (Figure 6B). Both t_{half} and $slope_{half}$ are affected more strongly by the initial amplitude of the potential of the extruding cell, its rest length, and tissue viscosity. The frequency of the extruding cell's potential has a minimal effect on the t_{half} but a strong effect on $slope_{half}$ compared to other parameters, indicating that the number of contractions affects extrusion dynamics differently than the strength of the contractions. Thus, in our model, the local microenvironment has only a moderate impact on extrusion dynamics.

DISCUSSION

Our computational model can represent oscillatory cell extrusion dynamics in a way that enables perturbations that cannot be made as precisely *in vivo*. Properties of the repulsive potential function of the extruding cell make large contributions to the morphogenesis of extruding cells, specifically time to half area loss (t_{half}) and slope of area loss ($slope_{half}$). Furthermore, changing tissue wide properties including viscosity and packing can enhance cell extrusion. Using our model, we observed how extrusion changes as non-autonomous properties, such as neighboring cell mechanics, are altered, even as we keep the extruding cell properties fixed. The biophysical properties and mechanics of the extruding cell have large effects on t_{half} and $slope_{half}$, with neighboring cell potential function parameters playing a less pronounced role. Our comparative analysis of model parameters and constraints suggest that biophysical features of the extruding cell such as the potential function and rest length, as well as tissue wide viscosity and packing contribute the most to t_{half} and $slope_{half}$. In particular, we find that smaller cells with higher amplitude area oscillations that are more confined or in a less viscous environment will be removed from the tissue faster than other cells. We suspect that more noise in cellular displacements disrupts coordinated contractions of neighboring cells due to their mechanical coupling. This further illustrates that the interaction between the potential-based mechanical coupling of cells and bulk tissue mechanics is a key effector of extrusion dynamics.

Active particle modeling together with hybrid tessellation enables variation of mechanical properties and observation of their impact on the homeostasis of epithelial cell sheets. Using this model, we can represent a diverse apical morphology of cells within an epithelium and manipulate both an extruding cell and its neighbors independently with well-defined and intuitive parameters under different conditions. With a common analysis pipeline, applied to both live and simulated cell timelapses, we can make comparisons between

these cases that were not previously possible. This type of model can be used to represent processes in a dynamic tissue, as opposed to more traditional models focused on static tissues with isodiametric cells. Our model overcomes previous limitations in modifying oscillatory dynamics of extruding cells,[39,42] and our data suggest autonomous contraction is a key contributor to extrusion of cells from epithelial tissues. These data are consistent with the apoptotic cell being an active physical participant in the process of cell extrusion.[40] During extrusion, an actomyosin ring forms in the extruding cell,[5] and pulses of contractile medio-apical actomyosin drive cell-autonomous constriction that contributes to cell expulsion,[6] similarly to observed ratcheting behaviors during apical constriction in *Drosophila*.[58,59] Contractility and rosette formation has been proposed to provide an essential mechanical signal to the surrounding cells by transiently increasing junctional tension and local cellular density.[40] While we do not define a period of stable oscillations in cell potential in our simulations, some simulated cells exhibit this feature, similar to observations of cells in living tissues (Figures 2D and S8). This emergent property suggests that cells may initially try to mechanically "resist" their neighbors' oscillations or the phase differences in neighboring cells may delay the start of the area loss process. We also see that extruding cells may "put up more of a fight" when their neighbors pulse more strongly, as the most mechanical resistance occurs for the highest neighbor oscillatory amplitude. Our results also provide additional support to the idea that the initial size/state of the cell may dictate the response to the environment (crowding) or damage (in this case, MTZ). Defining the autonomous features that promote extrusion could aid in predictions of cells primed to leave the tissue after a stimulus or during pathogenesis.

In our model, extrusion is not an emergent process—it is encoded in the function of the extruding cell's potential; however, area strain dynamics exhibit considerable diversity akin to observation of cells in living tissues. Elucidating factors that trigger extrusion *in vivo* may drive the development of future models where specific cell-intrinsic factors result in the emergence of extrusion. What are the molecular signals that drive this autonomous contraction program and extrusion in response to different stimuli? During apoptotic cell extrusion *in vivo*, caspase activation leads to enrichment of the bioactive lipid sphingosine-1-phosphate that regulates pulses to dictate regions of extrusion.[6] Caspase activation has also been shown to promote the disassembly of microtubules that is required for progression of extrusion.[60,61] Furthermore, a wave of calcium emanating from the apoptotic cell can induce polarized movement of the surrounding cells toward the extruding cells.[62] A current limitation of our computational model is the absence of molecular pathways that regulate specific phases of the extrusion process. Integration of known molecular regulatory components of actomyosin assembly/disassembly cycles that drive oscillatory dynamics into this active particle-based model will likely provide key insights into the removal of defective cells from homeostatic epithelial tissue maintenance.

While our data are supportive of oscillatory dynamics of an extruding cell providing the strongest contribution to the trajectory of extrusion, the neighboring cells still contribute, but to a lesser extent. Existing models representing contraction (without apoptosis) in other model systems note the strength of contractions as a pertinent parameter.[63,64] Contraction of the apoptotic cell also triggers a coordinated elongation of the neighboring cells, which requires E-cadherin-mediated cell-cell adhesion.[65] The small GTPase RhoA is a cadherin-dependent signal in the neighbor cells that becomes activated in response to contractile tension from the apoptotic cell.[7] However, in this study, changes in cell adhesion within the extruding cell or its neighbors were not directly accounted for. Therefore, it is plausible that the neighbors play a more significant role in facilitating the final removal phase than reflected by our model. Future studies using optogenetic manipulations of caspase activation, contractility, and adhesion in the extruding cell and its neighbors prior to elimination will provide additional clues on the mechanics of cell elimination during tissue homeostasis.

In summary, our computational model based on *in vivo* observations provides a tool to assess the contributions of the extruding cell and its neighbors to the process of eliminating defective cells from epithelial tissues. Given the conserved nature of epithelial topology and extrusion programs in different organisms, our model could provide insights into additional mechanisms such as ratcheting behaviors and guide future investigations into regulation of epithelial tissue homeostasis.

Limitations of the study

Limitations of this study include the challenges of matching computational simulations to noisy, non-stationary oscillatory functions representing *in vivo* cellular area strains. Our simulations are based on mechanical measures representing cellular contractility and adhesions and not individual components acting at sub-cellular scales. It is not possible to fully disentangle cellular and tissue mechanics due to mechanical coupling. We do not represent molecular feedback pathways proposed to be at play; however, we still find emergent properties matching cells from living tissues. Finally, extrusion events in the model are not emergent, which made it challenging to define unique phases of extrusion and prevents identification of events initiating this process. We hope that future models can build on this work and that these results can be used to guide further experimental interrogations of extrusion to provide greater insight into the mechanisms driving this crucial process and its dysregulation in pathological conditions.

RESOURCE AVAILABILITY

Lead contact

Further information and requests for resources and reagents should be directed to and will be fulfilled by the Lead Contact, L.D. (lad43@pitt.edu).

Materials availability

The transgenic zebrafish lines used in this paper are available from G.T.E. to other scientific researchers upon request.

Data and code availability

- **Data:** The published article includes all datasets and codes generated or analyzed during this study. Data supporting the findings presented can be found within the body of the paper and the supplemental information.
- **Code:** All custom code for the computational model and analyses have been deposited in the below Dataverse repository:
  Anjum, Sommer, 2024, "Data for "Assessing mechanical agency during apical apoptotic cell extrusion"", https://doi.org/10.7910/DVN/XKVWGA, Harvard Dataverse
- **Other items:** Additional information required to reanalyze the data reported in this paper is available from the lead contact upon request.

AUTHOR CONTRIBUTIONS

S.A.: Conceptualization, Software, Writing – Original Draft; L.T.: Investigation, Validation; Y.A.: Methodology, Conceptualization; G.T.E.: Conceptualization, Writing – Review and Editing, Project Administration, Supervision, Resources; L.A.D.: Conceptualization, Software, Writing – Review and Editing, Project Administration, Methodology.

DECLARATION OF INTERESTS

The authors declare no competing interests.

STAR★METHODS

Detailed methods are provided in the online version of this paper and include the following:

- KEY RESOURCES TABLE
- EXPERIMENTAL MODEL AND STUDY PARTICIPANT DETAILS
- METHOD DETAILS
  - Induction of extrusion in surface epithelial cells in larval zebrafish
  - Imaging of zebrafish larvae
  - Quantification of zebrafish cell area and polygon topology
  - Simulation and analysis pipeline
  - Hybrid tessellation technique
  - Local strain calculation
  - Developing a model with a larger field of cells and multiple extruding cells
- QUANTIFICATION AND STATISTICAL ANALYSIS

SUPPLEMENTAL INFORMATION

Supplemental information can be found online at https://doi.org/10.1016/j.isci.2024.111017.

REFERENCES

1. Rosenblatt, J., Raff, M.C., and Cramer, L.P. (2001). An epithelial cell destined for apoptosis signals its neighbors to extrude it by an actin- and myosin-dependent mechanism. Curr. Biol. *11*, 1847–1857. https://doi.org/10.1016/s0960-9822(01)00587-5.

2. Eisenhoffer, G.T., and Rosenblatt, J. (2013). Bringing balance by force: live cell extrusion controls epithelial cell numbers. Trends Cell Biol. *23*, 185–192. https://doi.org/10.1016/j.tcb.2012.11.006.

3. Eisenhoffer, G.T., Loftus, P.D., Yoshigi, M., Otsuna, H., Chien, C.B., Morcos, P.A., and Rosenblatt, J. (2012). Crowding induces live cell extrusion to maintain homeostatic cell numbers in epithelia. Nature *484*, 546–549. https://doi.org/10.1038/nature10999.

4. Katoh, H., and Fujita, Y. (2012). Epithelial homeostasis: elimination by live cell extrusion. Curr. Biol. *22*, R453–R455. https://doi.org/10.1016/j.cub.2012.04.036.

5. Villars, A., and Levayer, R. (2022). Collective effects in epithelial cell death and cell extrusion. Curr. Opin. Genet. Dev. *72*, 8–14. https://doi.org/10.1016/j.gde.2021.09.004.

6. Atieh, Y., Wyatt, T., Zaske, A.M., and Eisenhoffer, G.T. (2021). Pulsatile contractions promote apoptotic cell extrusion in epithelial tissues. Curr. Biol. *31*, 1129–1140.e4. https://doi.org/10.1016/j.cub.2020.12.005.

7. Duszyc, K., Gomez, G.A., Lagendijk, A.K., Yau, M.K., Nanavati, B.N., Gliddon, B.L., Hall, T.E., Verma, S., Hogan, B.M., Pitson, S.M., et al. (2021). Mechanotransduction activates RhoA in the neighbors of apoptotic epithelial cells to engage apical extrusion. Curr. Biol.

31, 1326–1336.e5. https://doi.org/10.1016/j.cub.2021.01.003.

8. Oakes, P.W., Wagner, E., Brand, C.A., Probst, D., Linke, M., Schwarz, U.S., Glotzer, M., and Gardel, M.L. (2017). Optogenetic control of RhoA reveals zyxin-mediated elasticity of stress fibres. Nat. Commun. *8*, 15817.

9. Davidson, L.A., Joshi, S.D., Kim, H.Y., von Dassow, M., Zhang, L., and Zhou, J. (2010). Emergent morphogenesis: elastic mechanics of a self-deforming tissue. J. Biomech. *43*, 63–70. https://doi.org/10.1016/j.jbiomech.2009.09.010.

10. Fletcher, A.G., Cooper, F., and Baker, R.E. (2017). Mechanocellular models of epithelial morphogenesis. Phil. Trans. R. Soc. B *372*, 20150519. https://doi.org/10.1098/rstb.2015.0519.

11. Weaire, D.L., and Hutzler, S. (2001). The Physics of Foams (Oxford University Press).

12. Staple, D.B., Farhadifar, R., Röper, J.C., Aigouy, B., Eaton, S., and Jülicher, F. (2010). Mechanics and remodelling of cell packings in epithelia. Eur. Phys. J. E Soft Matter *33*, 117–127. https://doi.org/10.1140/epje/i2010-10677-0.

13. Farhadifar, R., Röper, J.C., Aigouy, B., Eaton, S., and Jülicher, F. (2007). The influence of cell mechanics, cell-cell interactions, and proliferation on epithelial packing. Curr. Biol. *17*, 2095–2104.

14. Hashimoto, H., Robin, F.B., Sherrard, K.M., and Munro, E.M. (2015). Sequential contraction and exchange of apical junctions drives zippering and neural tube closure in a simple chordate. Dev. Cell *32*, 241–255. https://doi.org/10.1016/j.devcel.2014.12.017.

15. Fletcher, A.G., Osterfield, M., Baker, R.E., and Shvartsman, S.Y. (2014). Vertex models of epithelial morphogenesis. Biophys. J. *106*, 2291–2304. https://doi.org/10.1016/j.bpj.2013.11.4498.

16. Honda, H., Nagai, T., and Tanemura, M. (2008). Two different mechanisms of planar cell intercalation leading to tissue elongation. Dev. Dynam. *237*, 1826–1836.

17. Spahn, P., and Reuter, R. (2013). A vertex model of Drosophila ventral furrow formation. PLoS One *8*, e75051. https://doi.org/10.1371/journal.pone.0075051.

18. Rauzi, M., Verant, P., Lecuit, T., and Lenne, P.-F. (2008). Nature and anisotropy of cortical forces orienting Drosophila tissue morphogenesis. Nat. Cell Biol. *10*, 1401–1410.

19. Weliky, M., Minsuk, S., Keller, R., and Oster, G. (1991). Notochord morphogenesis in Xenopus laevis: simulation of cell behavior underlying tissue convergence and extension. Development *113*, 1231–1244.

20. Weliky, M., and Oster, G. (1990). The mechanical basis of cell rearrangement. I. Epithelial morphogenesis during Fundulus epiboly. Development *109*, 373–386.

21. Belmonte, J.M., Swat, M.H., and Glazier, J.A. (2016). Filopodial-Tension Model of Convergent-Extension of Tissues. PLoS Comput. Biol. *12*, e1004952. https://doi.org/10.1371/journal.pcbi.1004952.

22. Graner, F., and Glazier, J.A. (1992). Simulation of biological cell sorting using a two-dimensional extended Potts model. Phys. Rev. Lett. *69*, 2013–2016. https://doi.org/10.1103/PhysRevLett.69.2013.

23. Hirashima, T., Rens, E.G., and Merks, R.M.H. (2017). Cellular Potts modeling of complex multicellular behaviors in tissue morphogenesis. Dev. Growth Differ. *59*, 329–339. https://doi.org/10.1111/dgd.12358.

24. Wolff, H.B., Davidson, L.A., and Merks, R.M.H. (2019). Adapting a Plant Tissue Model to Animal Development: Introducing Cell Sliding into VirtualLeaf. Bull. Math. Biol. *81*, 3322–3341. https://doi.org/10.1007/s11538-019-00599-9.

25. Brodland, G.W., Yang, J., and Sweny, J. (2009). Cellular interfacial and surface tensions determined from aggregate compression tests using a finite element model. HFSP J. *3*, 273–281. https://doi.org/10.2976/1.3175812.

26. Chen, H.H., and Brodland, G.W. (2000). Cell-Level Finite Element Studies of Viscous Cells in Planar Aggregates. J. Biomech. Eng. *122*, 394–401. https://doi.org/10.1115/1.1286563.

27. Davidson, L.A., Oster, G.F., Keller, R.E., and Koehl, M.A. (1999). Measurements of Mechanical Properties of the Blastula Wall Reveal Which Hypothesized Mechanisms of Primary Invagination Are Physically Plausible in the Sea UrchinStrongylocentrotus purpuratus. Dev. Biol. *209*, 221–238. https://doi.org/10.1006/dbio.1999.9249.

28. Ramasubramanian, A., and Taber, L.A. (2008). Computational modeling of morphogenesis regulated by mechanical feedback. Biomech. Model. Mechanobiol. *7*, 77–91. https://doi.org/10.1007/s10237-007-0077-y.

29. Dalle Nogare, D., and Chitnis, A.B. (2020). NetLogo agent-based models as tools for understanding the self-organization of cell fate, morphogenesis and collective migration of the zebrafish posterior Lateral Line primordium. Semin. Cell Dev. Biol. *100*, 186–198.

30. Bi, D., Lopez, J.H., Schwarz, J.M., and Manning, M.L. (2015). A density-independent rigidity transition in biological tissues. Nat. Phys. *11*, 1074–1079. https://doi.org/10.1038/nphys3471.

31. Bi, D., Yang, X., Marchetti, M.C., and Manning, M.L. (2016). Motility-driven glass and jamming transitions in biological tissues. Phys. Rev. X *6*, 021011. https://doi.org/10.1103/PhysRevX.6.021011.

32. Armengol-Collado, J.M., Carenza, L.N., Eckert, J., Krommydas, D., and Giomi, L. (2023). Epithelia are multiscale active liquid crystals. Nat. Phys. *19*, 1773–1779. https://doi.org/10.1038/s41567-023-02179-0.

33. Moure, A., and Gomez, H. (2021). Phase-field modeling of individual and collective cell migration. Arch. Comput. Methods Eng. *28*, 311–344.

34. Marin-Riera, M., Brun-Usan, M., Zimm, R., Välikangas, T., and Salazar-Ciudad, I. (2016). Computational modeling of development by epithelia, mesenchyme and their interactions: a unified model. Bioinformatics *32*, 219–225. https://doi.org/10.1093/bioinformatics/btv527.

35. Sepulveda, N., Petitjean, L., Cochet, O., Grasland-Mongrain, E., Silberzan, P., and Hakim, V. (2013). Collective cell motion in an epithelial sheet can be quantitatively described by a stochastic interacting particle model. PLoS Comput. Biol. *9*, e1002944. https://doi.org/10.1371/journal.pcbi.1002944.

36. Palsson, E. (2001). A three-dimensional model of cell movement in multicellular systems. Future Generat. Comput. Syst. *17*, 835–852. https://doi.org/10.1016/S0167-739x(00)00062-5.

37. Misra, M., Audoly, B., Kevrekidis, I.G., and Shvartsman, S.Y. (2016). Shape Transformations of Epithelial Shells. Biophys. J. *110*, 1670–1678. https://doi.org/10.1016/j.bpj.2016.03.009.

38. Lin, L., Wang, X., and Zeng, X. (2014). Geometrical modeling of cell division and cell remodeling based on Voronoi tessellation method. Comput. Model. Eng. Sci.: Comput. Model. Eng. Sci. *98*, 203–220.

39. Marinari, E., Mehonic, A., Curran, S., Gale, J., Duke, T., and Baum, B. (2012). Live-cell delamination counterbalances epithelial growth to limit tissue overcrowding. Nature *484*, 542–545. https://doi.org/10.1038/nature10984.

40. Kuipers, D., Mehonic, A., Kajita, M., Peter, L., Fujita, Y., Duke, T., Charras, G., and Gale, J.E. (2014). Epithelial repair is a two-stage process driven first by dying cells and then by their neighbours. J. Cell Sci. *127*, 1229–1241.

41. Okuda, S., and Fujimoto, K. (2020). A Mechanical Instability in Planar Epithelial Monolayers Leads to Cell Extrusion. Biophys. J. *118*, 2549–2560. https://doi.org/10.1016/j.bpj.2020.03.028.

42. Monfared, S., Ravichandran, G., Andrade, J., and Doostmohammadi, A. (2023). Mechanical basis and topological routes to cell elimination. Elife *12*, e82435. https://doi.org/10.7554/eLife.82435.

43. Melo, S., Guerrero, P., Moreira Soares, M., Bordin, J.R., Carneiro, F., Carneiro, P., Dias, M.B., Carvalho, J., Figueiredo, J., Seruca, R., and Travasso, R.D.M. (2023). The ECM and tissue architecture are major determinants of early invasion mediated by E-cadherin dysfunction. Commun. Biol. *6*, 1132. https://doi.org/10.1038/s42003-023-05482-x.

44. Manning, M.L., and Collins, E.-M.S. (2015). Focus on physical models in biology: Multicellularity and active matter. New J. Phys. *17*, 040201.

45. Sanchez-Gutierrez, D., Tozluoglu, M., Barry, J.D., Pascual, A., Mao, Y., and Escudero, L.M. (2016). Fundamental physical cellular constraints drive self-organization of tissues. EMBO J. *35*, 77–88. https://doi.org/10.15252/embj.201592374.

46. Du, Q., Faber, V., and Gunzburger, M. (1999). Centroidal Voronoi tessellations: Applications and algorithms. SIAM Rev. *41*, 637–676. https://doi.org/10.1137/S0036144599352836.

47. Aurenhammer, F., and Edelsbrunner, H. (1984). An Optimal Algorithm for Constructing the Weighted Voronoi Diagram in the Plane. Pattern Recogn. *17*, 251–257. https://doi.org/10.1016/0031-3203(84)90064-5.

48. Gibson, M.C., Patel, A.B., Nagpal, R., and Perrimon, N. (2006). The emergence of geometric order in proliferating metazoan epithelia. Nature *442*, 1038–1041. https://doi.org/10.1038/nature05014.

49. van Leeuwen, I.M.M., Mirams, G.R., Walter, A., Fletcher, A., Murray, P., Osborne, J., Varma, S., Young, S.J., Cooper, J., Doyle, B., et al. (2009). An integrative computational model for intestinal tissue renewal. Cell Prolif. *42*, 617–636. https://doi.org/10.1111/j.1365-2184.2009.00627.x.

50. Paszek, M.J., and Weaver, V.M. (2004). The tension mounts: mechanics meets morphogenesis and malignancy. J. Mammary Gland Biol. Neoplasia *9*, 325–342. https://doi.org/10.1007/s10911-004-1404-x.

51. van Drongelen, R., Vazquez-Faci, T., Huijben, T.A.P.M., van der Zee, M., and Idema, T. (2018). Mechanics of epithelial tissue formation. J. Theor. Biol. *454*, 182–189. https://doi.org/10.1016/j.jtbi.2018.06.002.

52. Kaliman, S., Jayachandran, C., Rehfeldt, F., and Smith, A.-S. (2016). Limits of applicability of the voronoi tessellation determined by centers of cell nuclei to epithelium morphology. Front. Physiol. *7*, 551.

53. Chanet, S., Miller, C.J., Vaishnav, E.D., Ermentrout, B., Davidson, L.A., and Martin, A.C. (2017). Actomyosin meshwork mechanosensing enables tissue shape to orient cell force. Nat. Commun. *8*, 15014. https://doi.org/10.1038/ncomms15014.

54. Blanchard, G.B., and Adams, R.J. (2011). Measuring the multi-scale integration of mechanical forces during morphogenesis. Curr. Opin. Genet. Dev. *21*, 653–663. https://doi.org/10.1016/j.gde.2011.08.008.

55. Charrier, E.E., Pogoda, K., Wells, R.G., and Janmey, P.A. (2018). Control of cell morphology and differentiation by substrates with independently tunable elasticity and

viscous dissipation. Nat. Commun. *9*, 449. https://doi.org/10.1038/s41467-018-02906-9.

56. Murrell, M., Kamm, R., and Matsudaira, P. (2011). Substrate viscosity enhances correlation in epithelial sheet movement. Biophys. J. *101*, 297–306. https://doi.org/10.1016/j.bpj.2011.05.048.

57. Saltelli, A., Tarantola, S., and Chan, K.P.S. (1999). A Quantitative Model-Independent Method for Global Sensitivity Analysis of Model Output. Technometrics *41*, 39–56. https://doi.org/10.1080/00401706.1999.10485594.

58. Gorfinkiel, N., and Blanchard, G.B. (2011). Dynamics of actomyosin contractile activity during epithelial morphogenesis. Curr. Opin. Cell Biol. *23*, 531–539. https://doi.org/10.1016/j.ceb.2011.06.002.

59. Martin, A.C., Gelbart, M., Fernandez-Gonzalez, R., Kaschube, M., and Wieschaus, E.F. (2010). Integration of contractile forces during tissue invagination. J. Cell Biol. *188*, 735–749. https://doi.org/10.1083/jcb.200910099.

60. Valon, L., Davidović, A., Levillayer, F., Villars, A., Chouly, M., Cerqueira-Campos, F., and Levayer, R. (2021). Robustness of epithelial sealing is an emerging property of local ERK feedback driven by cell elimination. Dev. Cell *56*, 1700–1711.e8. https://doi.org/10.1016/j.devcel.2021.05.006.

61. Villars, A., Matamoro-Vidal, A., Levillayer, F., and Levayer, R. (2022). Microtubule disassembly by caspases is an important rate-limiting step of cell extrusion. Nat. Commun. *13*, 3632.

62. Takeuchi, Y., Narumi, R., Akiyama, R., Vitiello, E., Shirai, T., Tanimura, N., Kuromiya, K., Ishikawa, S., Kajita, M., Tada, M., et al. (2020). Calcium wave promotes cell extrusion. Curr. Biol. *30*, 670–681.e6.

63. Cavanaugh, K.E., Staddon, M.F., Munro, E., Banerjee, S., and Gardel, M.L. (2020). RhoA Mediates Epithelial Cell Shape Changes via Mechanosensitive Endocytosis. Dev. Cell *52*, 152–166.e5. https://doi.org/10.1016/j.devcel.2019.12.002.

64. Clement, R., Dehapiot, B., Collinet, C., Lecuit, T., and Lenne, P.F. (2017). Viscoelastic Dissipation Stabilizes Cell Shape Changes during Tissue Morphogenesis. Curr. Biol. *27*, 3132–3142.e3134. https://doi.org/10.1016/j.cub.2017.09.005.

65. Lubkov, V., and Bar-Sagi, D. (2014). Cadherin-Mediated Cell Coupling Is Required for Apoptotic Cell Extrusion. Curr. Biol. *24*, 868–874. https://doi.org/10.1016/j.cub.2014.02.057.

66. Eisenhoffer, G.T., Slattum, G., Ruiz, O.E., Otsuna, H., Bryan, C.D., Lopez, J., Wagner, D.S., Bonkowsky, J.L., Chien, C.B., Dorsky, R.I., and Rosenblatt, J. (2017). A toolbox to study epidermal cell types in zebrafish. J. Cell Sci. *130*, 269–277. https://doi.org/10.1242/jcs.184341.

67. Haas, P., and Gilmour, D. (2006). Chemokine signaling mediates self-organizing tissue migration in the zebrafish lateral line. Dev. Cell *10*, 673–680. https://doi.org/10.1016/j.devcel.2006.02.019.

68. Aigouy, B., Umetsu, D., and Eaton, S. (2016). Segmentation and Quantitative Analysis of Epithelial Tissues. Methods Mol Biol. *1478*, 227–239.

69. Herman, J., and Usher, W. (2017). SALib: an open-source Python library for sensitivity analysis. J. Open Source Softw. *2*, 97. https://doi.org/10.21105/joss.00097.

70. Anjum, S., Turner, L., Atieh, Y., Eisenhoffer, G.T., and Davidson, L. (2023). Assessing mechanical agency during apical apoptotic cell extrusion. Preprint at bioRxiv. https://doi.org/10.1101/2023.10.26.564227.

71. Westerfield, M. The Zebrafish Book; A guide for the laboratory use of zebrafish (Danio rerio). (2007).

72. Atieh, Y., Ruiz, O.E., and Eisenhoffer, G.T. (2021). Protocol for quantitative analysis of pulsatile contractions and cell extrusion in epithelial tissues of larval zebrafish. STAR Protoc. *2*, 100600. https://doi.org/10.1016/j.xpro.2021.100600.

73. Etournay, R., Merkel, M., Popović, M., Brandl, H., Dye, N.A., Aigouy, B., Salbreux, G., Eaton, S., and Jülicher, F. (2016). TissueMiner: a multiscale analysis toolkit to quantify how cellular processes create tissue dynamics. Elife *5*, e14334.

74. Sage, D., Prodanov, D., Tinevez, J.-Y. & Schindelin, J. in ImageJ User & Developer Conference.

75. Blanchard, G.B., Kabla, A.J., Schultz, N.L., Butler, L.C., Sanson, B., Gorfinkiel, N., Mahadevan, L., and Adams, R.J. (2009). Tissue tectonics: morphogenetic strain rates, cell shape change and intercalation. Nat. Methods *6*, 458–464. https://doi.org/10.1038/nmeth.1327.

STAR★METHODS

KEY RESOURCES TABLE

REAGENT or RESOURCE	SOURCE	IDENTIFIER
Chemicals, peptides, and recombinant proteins		
Metronidazole (MTZ)	Sigma	M-3761
Experimental models: Organisms/strains		
Zebrafish: *Et(Gal4-VP16)^{zc1044a}*; *Tg(UAS-E1b:nsfB-mCherry)*	Eisenhoffer et al.[66]	N/A
Zebrafish: *Tg(-8.0cldnB:lyn-EGFP)^{zf106}*	Haas and Gilmour[67]	N/A
Software and Algorithms		
Fiji	ImageJ	https://imagej.net/Fiji
Tissue Analyzer	Aigouy et al.[68]	https://grr.gred-clermont.fr/labmirouse/software/WebPA/index.html
Prism version 8	GraphPad	https://www.graphpad.com/scientific-software/prism/
MATLAB	MathWorks	https://www.mathworks.com/products/matlab.html
SA Lib	Herman and Usher[69]	https://salib.readthedocs.io/en/latest/index.html
Custom code	Anjum et al.[70]	https://doi.org/10.7910/DVN/XKVWGA

EXPERIMENTAL MODEL AND STUDY PARTICIPANT DETAILS

Experiments were conducted on 4 dpf larval zebrafish (*Danio rerio*) maintained under standard laboratory conditions with a cycle of 14 h of light and 10 h of darkness. Larvae were collected and kept in E3 larva medium at 28.5°C.[71] The zebrafish used in this study were handled in accordance with the guidelines of the University of Texas MD Anderson Cancer Center Institutional Animal Care and Use Committee.

METHOD DETAILS

Induction of extrusion in surface epithelial cells in larval zebrafish

4dpf larvae were treated with 10mM metronidazole (MTZ) for 2–4 h in a 28.5°C incubator to induce extrusion activity.[6,72]

Imaging of zebrafish larvae

4 dpf zebrafish larvae were anesthetized with 0.04% tricaine in E3 and mounted in an X-plate Petri dish with using 0.5% UltraPure Low Melting Point Agarose and E3. The larvae were imaged on a ZEISS LSM 800 laser scanning confocal microscope with fluorescent channels set to a wavelength of 488 nm and 561 nm. Images were acquired from 30 s, 1 min or 1 min and 30 s acquisition times.

Quantification of zebrafish cell area and polygon topology

The resulting confocal images were handled in Fiji and segmented and the resulting area and polygon topology were assessed using Tissue Analyzer[73] as described in the previous protocols paper.[6]

Simulation and analysis pipeline

The simulation is coded as an ImageJ macro to allow pixel manipulation and visualization. We have developed a lattice-free model of an epithelial sheet. Cells are described as nodes that are initialized randomly within a square bounding box. Corner nodes are fixed, while border nodes move along one axis, and interior nodes may move along both axes. Nodes interact with each other by repelling neighbors via a nonlinear compressive spring maintaining cell areas. Cell movement is governed by a force balance enforcing Langevin dynamics, incorporating stochasticity and drag forces from viscous media.[49] At the beginning of the simulation, cells are randomly assigned uniformly distributed potentials/rest lengths. These rest lengths determine how much cells repel neighboring cells, as a function of distance. The repulsion force is scaled by viscosity μ and the simulation is advanced using forward Euler methods. When cells are first initialized, they move more because of their proximity causing more force due to their random placement. We allow 100 timesteps for the cell positions to equilibrate before performing manipulations. An extruding cell is selected from centroids in the center of the field at random, and centroids within a pixel based radius are selected to be the neighboring cells and assigned an oscillatory potential as well, with oscillations randomized to begin within the first ten timesteps after equilibration is complete. Extruding cells adopt their linearly decreasing sinusoidal potential right away. They are removed from the simulation when their potential function drops below 0.01. After tessellation using the hybrid CVT method, segmentation of the cells is performed via ImageJ using cell centroid information derived from the model and assigning unique pixel values to

cells detected as particles after tessellation. We extract morphometric features using regions of interest (ROIs) from each frame of the simulation (typically 60–70 frames). Sidedness is calculated for cells not on the boundaries of the simulation by expanding the ROI and finding unique pixel intensities. We calculate strain from ROI measurements for cells over time using MATLAB (Mathworks). To calculate the slope and time to half area loss, we calculate the lower Hilbert envelope by using the discrete Fourier transform on the analytic signal of the strain data (Figure S6). The envelope in the neighborhood of half area loss is used to calculate the slope and interpolate the time at which half area loss is achieved. The absolute time to half area loss is calculated first, and then the troughs prior to this time and after this time are identified. A line is drawn between these two points. We interpolate back to the time axis using this line to estimate the time to half area loss (t_{half}). The slope of this line is recorded as the slope at half area loss ($slope_{half}$). This approach was chosen to lower bias of half area loss times to changes in amplitude and frequencies of the driving potential. Statistical analysis is performed in MATLAB and GraphPad Prism 9. To speed up the simulation and analysis pipeline, we used MATLAB-ImageJ.[74] By running ImageJ via MATLAB, simulations could be run in sequence without jumping from MATLAB to ImageJ between simulation and analysis phases. The simulation and analysis pipeline overview is provided (Figure S1).

Hybrid tessellation technique

We developed a method of tessellating cells that represents the physics of the system better than a Voronoi tessellation. The Voronoi tessellation is done purely based on the location of the cell centroids. First, a Delaunay triangulation is performed, and the circumcenters of these triangles are connected to form the Voronoi tessellation. In our new method, we calculate the centroid of the triangle, weighted by the resting lengths of the cells that form the triangle. We average this with the original Voronoi circumcenter. This enables us to represent cellular extrusion by dramatically lowering a cell's resting length in the simulation and inflating this value during the tessellation to bias the weighted centroid toward an extruding cell. A shortcoming is sudden T1-type flips of edges in the network that occur when the weighted circumcenter moves outside of the Delaunay triangle. We can attribute this to the special case in which the circumcenter of the Delaunay triangle lies outside the triangle itself and when Delaunay triangles undergo large configuration changes. Due to this instability, we sought to find the best of both worlds. We tested weighted combinations of the Voronoi tessellation (VT) and the Weighted Centroidal Voronoi (weighted CVT) tessellation. The combination that allowed for the greatest stability while still being able to satisfy our base case criteria was an even (50% each) weighting of the Voronoi tessellation and weighted CVT, which we call the Hybrid Centroidal Voronoi tessellation (hybrid CVT). This method allows removal of cells in a way that can be precisely controlled.

$$x_{centroid} = \frac{\frac{x_i}{rest_i} + \frac{x_j}{rest_j} + \frac{x_k}{rest_k}}{\frac{1}{rest_i} + \frac{1}{rest_j} + \frac{1}{rest_k}}$$

Each index (i, j, k) represents a node of a Delaunay triangle. This tessellation is implemented via modification of the Delaunay Voronoi ImageJ plugin.

Local strain calculation

During exploratory simulations of oscillatory extrusion, strain of a local neighborhood of cells was examined in addition to cellular strain. This designation of a local "corona" is inspired by Tissue Tectonics.[75] The deformation gradient matrix F is derived from the equation of an ellipse fitted to the ROI of a cell or its neighborhood (Figure S9A) and is used to calculate Lagrangian finite strains, shown in Figure S9.

We define the initial configuration of the ellipse (fitted to either the cell or corona) at t = 0 as:

$$(Ax+By)^2 + (Cx+Dy)^2 = 1$$

The same ellipse after deformation, at t = 1 is defined as:

$$(ax+by)^2 + (cx+dy)^2 = 1$$

Using the deformation gradient tensor **F**, we map the initial configuration of the ellipse to its current configuration and solve for **F**:

$$\begin{bmatrix} A & B \\ C & D \end{bmatrix} = \begin{bmatrix} a & b \\ c & d \end{bmatrix} * F$$

$$F = \begin{bmatrix} a & b \\ c & d \end{bmatrix}^{-1} \begin{bmatrix} A & B \\ C & D \end{bmatrix}$$

We then calculate the Lagrangian finite strain tensor for both the cell and corona levels.

$$\varepsilon = \frac{1}{2}\left(F^T F - I\right) = \begin{bmatrix} \varepsilon_{xx} & \varepsilon_{xy} \\ \varepsilon_{yx} & \varepsilon_{yy} \end{bmatrix}$$

The x and y directions of cell strains (Cell ε_{xx} and Cell ε_{yy}) were essentially equivalent and close to half of the cell area strain, so we chose to show only cell area strain for clarity. The area strains are calculated from the pixels contained in the cells within the ROIs, rather than using the ellipse areas for more precise measurements. The local strains of a cell, its neighbors, and its neighbor's neighbors (2-level corona; Local ε_{xx}, Local ε_{yy}, Local Cell ε_{area}) were negligible, even in the case where only the extruding cell potential was oscillating despite it reaching half area loss sooner (Figures S9A, S9C, and S9D). We expect that this is due to area conservation: when a cell has a shrinking area, the neighboring cell takes on that area. This is not a perfect 1:1 area allocation as viscous drag forces delay area allocations as a function of force dampening within the media. This is an interesting observation in that extruding cell oscillations may have a varying effect on the deformation of nearby cells. In conjunction with possible minimal autonomous oscillations of non-extruding cells, we suspect that oscillations may be triggered later on with compounding of these forces.

Developing a model with a larger field of cells and multiple extruding cells

The modeling results shown involve a model representing a single cell oscillating in a small field of cells to isolate the effects of the mechanical properties studied and establish case-by-case independence on our statistical analysis. However, *in vivo*, multiple cells oscillate within a larger field. Another version of the model involves a larger field of approximately 400 cells wherein five cells are designated as oscillatory extruding cells (Figure S10). The extruding cells are within the center third of the field to minimize boundary effects. This adds a layer of complexity, as oscillations from one extruding cell, in close enough proximity to the neighborhood of another extruding cell, may impact the dynamics of that extruding cell, as well as the morphology of its neighbors. This extended model is more computationally expensive but allows a way to probe tissue-scale mechanics of propagating oscillations more directly.

QUANTIFICATION AND STATISTICAL ANALYSIS

To extract amplitudes from the area strain trajectories, we calculate the Hilbert envelope by using the discrete Fourier transform on the analytic signal of the strain data. Amplitude is calculated as half the difference between adjacent peaks and troughs in the signal for live cell and simulated data (Figure S6). For comparisons between two groups such as the amplitudes for matching the base case, we used the Wilcoxon rank-sum test at the 95% significance level in MATLAB. For analysis of manipulated features such as amplitude, frequency, and packing, we use a one-way ANOVA to compare variations across groups at the 95% significance level using GraphPad Prism. We checked normality of the distribution of half times as well as the residuals, and our data meets criteria for sufficient samples to account for deviations from normality. All data is represented as mean and 95% confidence interval. Sample sizes may be found in the text and figure legends.

For the attribution of features of time to half area loss, we performed global sensitivity analysis using the extended Fourier Amplitude Sensitivity test (eFAST) using the SALib package in Python.[69] The eFAST test leverages periodic sampling within the parameter intervals to detect peaks in the output data that are attributed to these signals by computing the Fourier transform. This informs calculation of Sobol indices by measuring the fraction of the variance in the output attributed to Fourier coefficients associated with each of the varied parameters. We used 480 parameter sets generated by the SA Lib fast sampler and ran as many simulations to extract our two outputs. These indices tell us the fraction by which the variation of the summary statistic would be reduced if a parameter was held constant. Together, the effects of synergy between changing multiple parameters are shown. Results are interpreted as contributions to variability in the output variables of time to half area loss and slope of area loss, with larger values indicating a greater contribution.